Porous Au Nanoparticles with Tunable Plasmon Resonances and Intense Field Enhancements for Single-Particle SERS

4 AUTHORS, INCLUDING:

Qingfeng Zhang
University of South Carolina
13 PUBLICATIONS **166** CITATIONS

SEE PROFILE

Nicolas Large
Northwestern University
42 PUBLICATIONS **607** CITATIONS

SEE PROFILE

Hui Wang
University of South Carolina
34 PUBLICATIONS **385** CITATIONS

SEE PROFILE

Porous Au Nanoparticles with Tunable Plasmon Resonances and Intense Field Enhancements for Single-Particle SERS

Qingfeng Zhang,[†] Nicolas Large,[‡] Peter Nordlander,[‡] and Hui Wang*,[†]

[†]Department of Chemistry and Biochemistry, University of South Carolina, 631 Sumter Street, Columbia, South Carolina 29208, United States

[‡]Department of Physics and Astronomy, Department of Electrical and Computer Engineering, and Laboratory for Nanophotonics, Rice University, Houston, Texas 77005, United States

S *Supporting Information*

ABSTRACT: Porous Au nanoparticles with fine-controlled overall particle sizes have been fabricated using a kinetically controlled seed-mediated growth method. In contrast to spherical Au nanoparticles with smooth surfaces, the porous Au nanoparticles exhibit far greater size-dependent plasmonic tunability and significantly intensified local electric field enhancements exploitable for single-particle plasmon-enhanced spectroscopies. The effects of the nanoscale porosity on the far- and near-field optical properties of the nanoparticles have been investigated both experimentally by optical extinction and single-nanoparticle Raman spectroscopic measurements and theoretically through finite-difference time-domain calculations.

SECTION: Plasmonics, Optical Materials, and Hard Matter
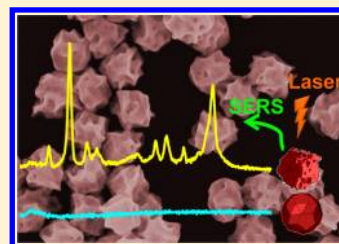
Noble metal nanoparticles exhibit intriguing plasmon-dominated optical properties.[1−3] By judiciously tailoring the geometries of the metal nanoparticles, one can fine-tune the optical resonance frequencies and optimize the electric near-field enhancements associated with the plasmonic excitations.[2−6] Expanding the plasmonic tunability of nanoparticles over a broad spectral range is of paramount importance because it opens up a whole set of new opportunities for photonic,[7,8] optoelectronic,[9,10] spectroscopic,[11,12] and biomedical applications.[13,14] This has, in turn, stimulated rapidly growing interests in a variety of metallic nanostructures with geometrically tunable optical properties, such as nanorods,[2,15] nanoprisms,[16,17] nanoshells,[18] and nanocages.[19] Here, we report a new class of metallic nanostructures, porous Au nanoparticles, which combine highly tunable plasmon resonances and intense local electric field enhancements exploitable for single-particle surface-enhanced Raman spectroscopy (SERS).

Two-dimensional mesoporous or nanoporous Au thin films[20] have been of tremendous interest due to their interesting porosity-dependent optical properties[21−23] and superior catalytic activities.[24−26] While a planar Au thin film only supports propagating surface plasmon waves, it has been demonstrated that the excitation of both propagating and localized plasmon resonances can be achieved in nanoporous Au membranes.[23] In this context, the large local field enhancements associated with the localized plasmon modes sustained by the nanoporous films can be harnessed for SERS-based molecular characterization and sensing applications.[27,28] For finite Au nanoparticles whose plasmons are already localized, how the nanoscale porosity influences the optical properties of the particles still remains unknown. Although smooth spherical nanoparticles (SSNPs) of Au or Ag possess

well-defined localized plasmon resonances in the visible region, their plasmonic tuning range is rather limited. Here, we show that Au porous nanoparticles (PNPs) exhibit greatly enhanced plasmonic tunability over a much broader spectral range with significantly intensified near-field enhancements in comparison to the SSNPs of the same sizes. We demonstrate, both experimentally and theoretically, that introducing nanoscale porosity to a Au nanoparticle has profound influence on both the far- and near-field optical properties of the particle.

The Au PNPs were fabricated through a seed-mediated growth process in aqueous solution at room temperature (see experimental details in the Supporting Information). Briefly, colloidal Au seeds were prepared by reducing chloroauric acid ($HAuCl_4$) with sodium borohydride ($NaBH_4$) in the presence of cetyltrimethylammonium chloride (CTAC). The growth of the Au PNPs was initiated by injecting various volumes of diluted Au seeds into the particle growth solution, which contained $HAuCl_4$, L-ascorbic acid (AA), and CTAC. The reaction solution was gently mixed immediately after the addition of Au seeds and then left undisturbed at room temperature for 4 h. The as-fabricated particles were separated from the reaction mixtures through centrifugation and redispersion in water. Figure 1A shows a representative scanning electron microscopy (SEM) image of the as-fabricated Au PNPs with diameters of 189 ± 8 nm. Each individual particle appeared to be highly porous with nanoscale pores in the range of 10−40 nm randomly distributed over the particle surfaces. The nanoporosity of the particles was more clearly
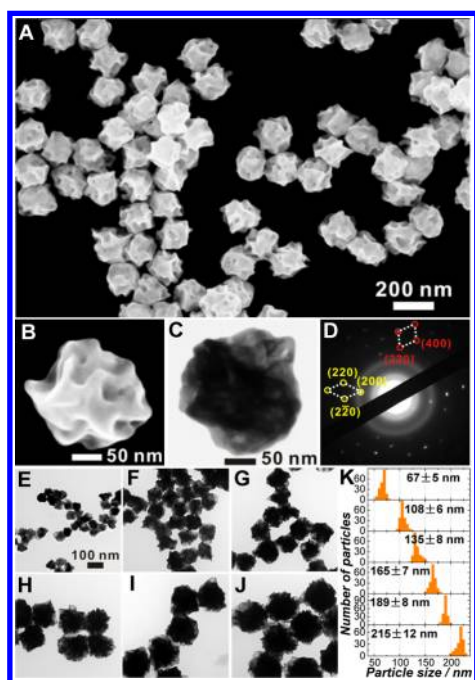
Figure 1. (A) SEM image of Au PNPs with an average size of 189 nm. (B) SEM image and (C) TEM image of an individual Au PNP. (D) SAED pattern obtained from the particle in panel C. (E−J) TEM images of Au PNPs of various average sizes fabricated by adding (E) 0.5, (F) 0.1, (G) 0.05, (H) 0.025, (I) 0.015, and (J) 0.01 mL of Au seed solution. Panels E−J share the same scale bar in panel E. (K) Histograms showing the size distribution of the Au PNPs shown in panels E−J.

Figure 2. (A) Schematics illustrating the morphology control of Au nanocrystals through controlling the particle growth kinetics. (B) SEM image of Au QS nanoparticles. The inset highlights one individual particle. (C) TEM image of one Au QS nanoparticle. (D) SAED pattern obtained from the particle in panel C. (E) SEM image of Au TOH nanoparticles. The inset highlights one individual nanoparticle. (F) TEM image of one Au TOH nanoparticle. (G) SAED pattern obtained from the particle in panel F.

visualized in the high-magnification SEM and transmission electron microscopy (TEM) images taken on individual particles, as shown in Figure 1B and C, respectively. Figure 1D shows the corresponding selected area electron diffraction (SAED) pattern of the particle shown in Figure 1C, which indicated that each PNP was polycrystalline in nature and was composed of crystalline domains that adopted different orientations.

The average size of the particles can be fine-controlled in the range from ∼50 nm to sub-μm by simply adjusting the amount of Au seeds added into the growth solution. As shown in Figure 1E−J, the average sizes of the PNPs increased as the volume of the Au seeds decreased. The particles were highly monodisperse with narrow size distribution, as shown in Figure 1K. Unlike some other seed-mediated growth methods through which the nanoparticles evolve into different morphologies as the overall particle size varies,[29,30] the nanoscale porous morphology of the particles fabricated using this protocol was well-preserved throughout the whole particle size tuning range. Although the average size of the pores appeared to be independent on the overall particle size, the average numbers of pores on individual Au PNPs were observed to increase with the overall particle sizes, as further shown in Figure S1 in the Supporting Information.

The kinetics of the seed-mediated particle growth was found to be a key factor in determining the morphology of the resulting nanoparticles. Figure 2A schematically illustrates the correlation between particle morphologies and the reaction kinetics. By adding HCl into the particle growth solution, the growth of nanoparticles could be significantly slowed down due to the decreased reducibility of AA in acidic environment,[31]
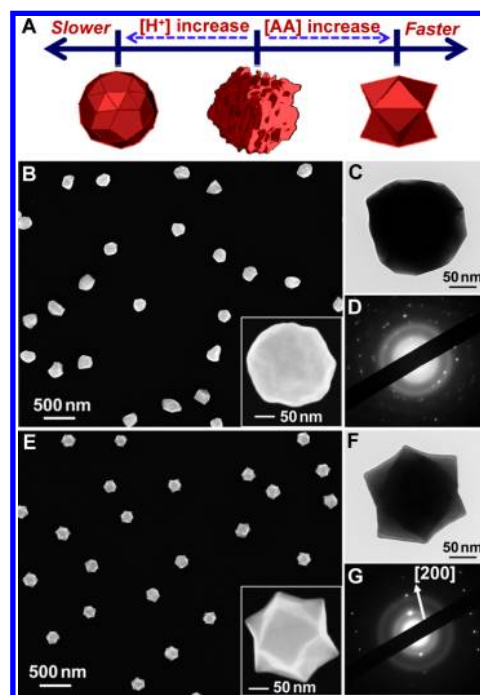
leading to the formation of Au quasi-spherical (QS) nanoparticles (Figure 2B), which are thermodynamically more stable than the PNPs. The TEM image (Figure 2C) and SAED pattern (Figure 2D) of an individual particle clearly show that each Au QS particle was polycrystalline with several crystalline domains packed together into a multitwined structure. The nanoparticle growth process could be significantly accelerated by increasing the amount of AA added to the particle growth solution. The faster particle growth facilitated the formation of the kinetically favored, single-crystalline Au trisoctahedral (TOH) nanoparticles enclosed by 24 high-index {221} facets[32] (see Figure 2E and F). The SAED pattern of an individual TOH particle (Figure 2G) confirmed the single-crystalline nature of the particle. In this context, the Au PNPs can be considered as a unique "metastable" product resulting from the intermediate particle growth kinetics that fall between the thermodynamically controlled regime and kinetically favored regime.

The Au PNPs exhibit size-dependent localized plasmon resonances whose frequencies are highly tunable across the visible and near-IR spectral regions. As shown in Figure 3A, the plasmon resonance progressively red-shifted and became increasingly broadened as the overall particle size increased. In comparison to the Au QS particles with similar sizes, the PNPs exhibited significantly enhanced plasmonic tunability over a much broader spectral range. For SSNPs within the quasi-static limit (diameters smaller than ∼60 nm), the plasmon resonance wavelengths lie around 520 nm and are essentially independent of particle size. As the size of a SSNP increases to the size regime beyond the quasi-static limit, the dipole plasmon mode starts to red shift and becomes
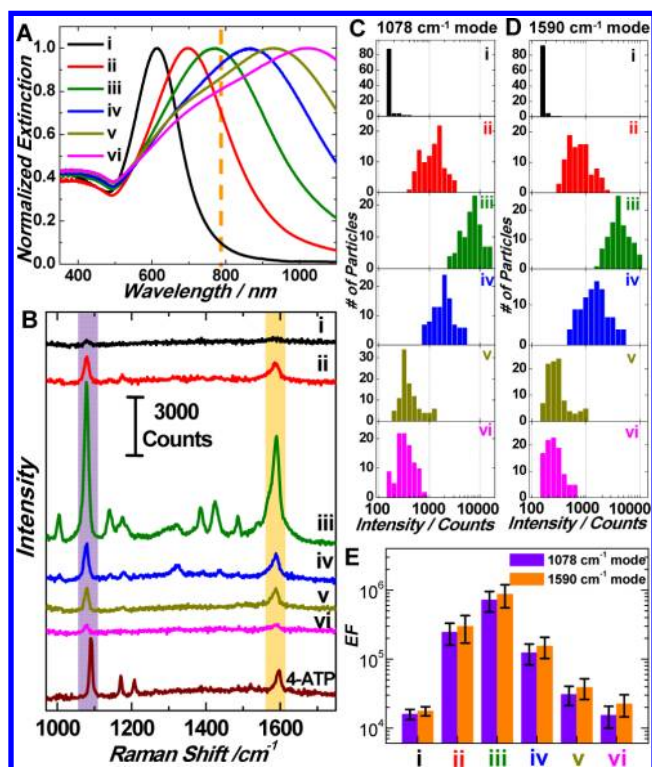
Figure 3. (A) Extinction spectra of colloidal Au PNPs of various sizes. The vertical dashed line shows the excitation laser wavelength (785 nm) for Raman measurements. (B) Representative SERS spectra of 4-ATP adsorbed on individual Au PNPs of various sizes. The bottom spectrum is the normal Raman spectrum of the neat 4-ATP film. Histograms of the Raman intensity of the (C) 1078 and (D) 1590 cm^{-1} modes obtained from individual Au PNPs. (E) Average SERS EFs on individual Au PNPs of various sizes. The labels of i, ii, iii, iv, v, and vi in all of the panels correspond to the Au PNP samples shown in Figure 1E–J, respectively.

significantly broadened. In addition, the multipolar plasmon modes, such as quadrupole, octupole, and even higher order multipole modes, become increasingly pronounced and begin to dominate the overall extinction spectral line shapes as a consequence of the phase-retardation effects.[33,34] We have experimentally demonstrated such size dependence of the plasmonic features by measuring the extinction spectra of Au QS particles with various sizes (Figure S2 in the Supporting Information). For the Au TOH particles with a side length of 94 ± 4 nm, a strong quadrupole mode together with a broad, weaker dipole plasmon band was also observed in the extinction spectrum (Figure S3A in the Supporting Information). Remarkably, when nanoscale porosity was introduced into the Au nanoparticles, the higher-order mode (quadrupole) was significantly dampened, whereas the dipole plasmon mode remained robust and shifted to longer wavelengths.

In addition to the greatly enhanced tunability of the far-field optical responses, the nanoscale porosity also creates sharp, nanoscale surface features, giving rise to intense near-field "hot spots" upon plasmonic excitation. The Au PNPs thus combine highly tunable plasmon resonances with intense local field enhancements, allowing for single-particle SERS under near-IR excitation (785 nm). 4-Aminothiophenol (4-ATP) was used as a nonresonant probe molecule to evaluate the overall Raman enhancements on individual Au PNPs. A submonolayer of isolated particles was immobilized on a polyvinylpyridine-

functionalized silicon substrate and was used as the SERS substrates (see Figure S4 in the Supporting Information). We used a confocal Raman microscope to collect the SERS spectra one particle at a time. SERS spectra were collected from more than 100 individual particles for each sample. Figure 3B shows the representative normal Raman spectrum of 4-ATP and SERS spectra of 4-ATP adsorbed on individual PNPs. The SERS signal was the largest when the plasmon was resonant with the laser and gradually decreased as the plasmon resonances were detuned from the laser. The plasmon-dependent SERS activity was further confirmed by the histograms of the Raman intensities of the 1078 and 1590 cm^{-1} modes obtained from 100 individual particles (Figure 3C and D) for each sample. The Raman enhancement factors (EFs) were estimated to be on the order of 10^5, approaching 10^6 when the plasmon resonance was resonant with the excitation laser. These estimated EFs were averaged over the entire particle surfaces. The local enhancements in the near-field hot spots, however, are anticipated to be at least 1 order of magnitude higher. In contrast, the Au QS and TOH particles exhibited much weaker Raman enhancements than the PNPs (see Figures S2I and S3B-D in the Supporting Information).

To gain more quantitative insights into the structure–property relationship of the nanoporous particles, finite-difference time-domain (FDTD) simulations were performed to calculate their extinction spectra and near-field enhancements (see details in the Supporting Information). Figure 4A shows the calculated extinction spectra of a Au sphere (189 nm in diameter) with a varying number of pores randomly generated at the particle surface. Both the dipole and quadrupole plasmon bands progressively red-shifted upon an increase of the porosity. As the number of nanoscale pores increased, the intensity of the quadrupole mode gradually decreased while the dipole plasmon mode remained robust (Figure 4B). The effects of nanoporosity on the far-field optical extinction of the particles were also found to be size-dependent. As shown in Figure S5 in the Supporting Information, for relatively small Au particles within the quasi-static limit, the nanoscale porosity caused a decrease of the dipolar extinction peak and a broadening and red shift with increasing number of pores. Larger particles exhibit greatly enhanced tunability of the dipole resonance, with higher-order multipolar resonances significantly dampened. In Figure 4C and D, we compare the calculated extinction spectra of Au PNPs and SSNPs with various overall sizes. It is apparent that the plasmon resonance frequencies became much more sensitively dependent on the overall size of the PNPs than those of the SSNPs. The FDTD results showed excellent agreement with our experimental observations.

We have further used FDTD to calculate the near-field enhancements of the particles. Figure 4E shows the cross-sectional views of the calculated near-field distributions ($|E/E_0|^2$) of PNP and SSNP with various sizes at 785 nm excitation. Each PNP possesses large numbers of hot spots with local field enhancements significantly more intense than those achievable on the SSNP of the same overall size. As shown in Figure 4F and G, the average near-field intensity ($|E/E_0|^2$) enhancements of Au PNP were about 10 times higher than those on the SSNP. The Au TOH particle with a side length of 94 nm (Figure S6 in the Supporting Information) showed larger near-field enhancements than the SSNPs largely due to the presence of sharp tips at the particle surfaces. This is in agreement with the experimental observations that the Raman enhancements
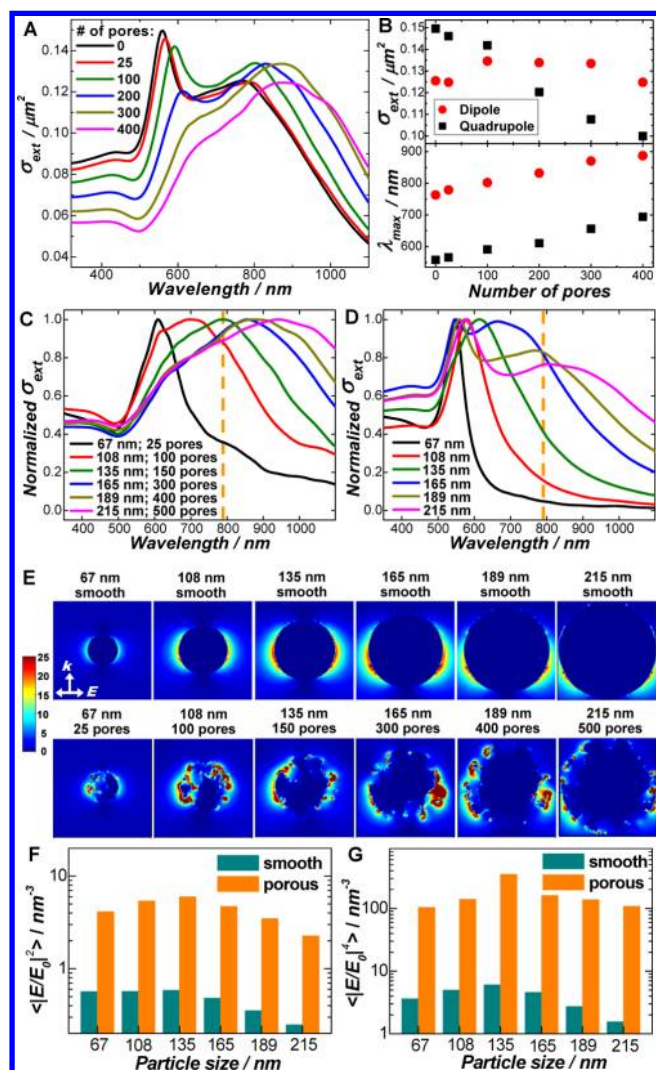
Figure 4. (A) Calculated extinction spectra of spherical Au particles (189 nm in diameter) with 0, 25, 100, 200, 300, and 400 pores. (B) Calculated extinction cross sections at the dipole and quadrupole resonance wavelengths (upper panel) and the plasmon resonance wavelengths (lower panel) of the Au particles (189 nm) with a varying number of pores. Calculated extinction spectra of (C) Au PNPs and (D) Au SSNPs of different particle sizes. The particle sizes and the numbers of pores in each particle are labeled in panel C. (E) The cross-sectional views of the calculated near-field enhancements $|E/E_0|^2$ of SSNPs (upper row) and PNPs (lower row) with various sizes at 785 nm excitation. Mean-field enhancements averaged over volume: (F) $\langle|E/E_0|^2\rangle$ and (G) $\langle|E/E_0|^4\rangle$ of PNPs and SSNPs of overall particle sizes of 67, 108, 135, 165, 189, and 215 nm.

on individual TOH particles were higher than those on the Au QS nanoparticles (see Figures S2I and S3B in the Supporting Information), though they were not as high as those achieved on individual Au PNPs.

In summary, kinetically controlled seed-mediated growth allows for the fabrication of nanoscale porous Au particles with fine-controlled overall particle sizes. The nanoporous Au particles represent a new class of subwavelength photonic materials that combine tunable localized plasmon resonances with intense near-field enhancements exploitable for single-particle SERS. In addition to their attractive optical properties, nanoporous Au may also exhibit superior catalytic activities toward a variety of chemical reactions, as previously

demonstrated on nanoporous Au films.[24−26] Therefore, these optically tunable porous nanoparticles may serve a dual purpose, as substrates for plasmon-enhanced spectroscopies and efficient surface catalysts. This dual functionality may allow for quantitative spectroscopic studies of kinetics and reaction pathways of surface-catalyzed reactions with unprecedented sensitivity and detail.

■ ASSOCIATED CONTENT

S **Supporting Information**

Experimental details and additional figures as noted in the text, including chemicals and materials, synthesis of Au seeds, Au porous nanaparticles, Au trisoctahedral nanoparticles, characterizations, single-particle SERS measurements, enhancement factor calculations, finite-difference time-domain calculations, SEM images of Au porous nanaparticles, TEM images of quasi-spherical Au nanoparticles, experimental extinction spectrum of colloidal trisoctahedral Au nanoparticles, representative SERS spectra, schematic illustration of the single-particle SERS measurements, dark-field optical image and SEM image, and calculated extinction spectra. This material is available free of charge via the Internet at http://pubs.acs.org.

■ AUTHOR INFORMATION

Corresponding Author

*E-mail: wang344@mailbox.sc.edu. Phone: 803-777-2203. Fax: 803-777-9521.

Notes

The authors declare no competing financial interest.

■ REFERENCES

(1) Halas, N. J.; Lal, S.; Chang, W. S.; Link, S.; Nordlander, P. Plasmons in Strongly Coupled Metallic Nanostructures. *Chem. Rev.* **2011**, *111*, 3913−3961.

(2) Murphy, C. J.; San, T. K.; Gole, A. M.; Orendorff, C. J.; Gao, J. X.; Gou, L.; Hunyadi, S. E.; Li, T. Anisotropic Metal Nanoparticles: Synthesis, Assembly, and Optical Applications. *J. Phys. Chem. B* **2005**, *109*, 13857−13870.

(3) Jain, P. K.; Huang, X. H.; El-Sayed, I. H.; El-Sayed, M. A. Noble Metals on the Nanoscale: Optical and Photothermal Properties and Some Applications in Imaging, Sensing, Biology, and Medicine. *Acc. Chem. Res.* **2008**, *41*, 1578−1586.

(4) Burda, C.; Chen, X. B.; Narayanan, R.; El-Sayed, M. A. Chemistry and Properties of Nanocrystals of Different Shapes. *Chem. Rev.* **2005**, *105*, 1025−1102.

(5) El-Sayed, M. A. Some Interesting Properties of Metals Confined in Time and Nanometer Space of Different Shapes. *Acc. Chem. Res.* **2001**, *34*, 257−264.

(6) Xia, Y. N.; Halas, N. J. Shape-Controlled Synthesis and Surface Plasmonic Properties of Metallic Nanostructures. *MRS Bull.* **2005**, *30*, 338−344.

(7) Lal, S.; Link, S.; Halas, N. J. Nano-Optics from Sensing to Waveguiding. *Nat. Photonics* **2007**, *1*, 641−648.

(8) Oulton, R. F.; Sorger, V. J.; Zentgraf, T.; Ma, R. M.; Gladden, C.; Dai, L.; Bartal, G.; Zhang, X. Plasmon Lasers at Deep Subwavelength Scale. *Nature* **2009**, *461*, 629−632.

(9) Knight, M. W.; Sobhani, H.; Nordlander, P.; Halas, N. J. Photodetection with Active Optical Antennas. *Science* **2011**, *332*, 702−704.

(10) Ferry, V. E.; Munday, J. N.; Atwater, H. A. Design Considerations for Plasmonic Photovoltaics. *Adv. Mater.* **2010**, *22*, 4794−4808.

(11) Willets, K. A.; Van Duyne, R. P. Localized surface plasmon resonance spectroscopy and sensing. In *Annual Review of Physical Chemistry*; Annual Reviews: Palo Alto, CA, 2007; Vol. *58*, pp 267−297.

(12) Camden, J. P.; Dieringer, J. A.; Zhao, J.; Van Duyne, R. P. Controlled Plasmonic Nanostructures for Surface-Enhanced Spectroscopy and Sensing. *Acc. Chem. Res.* **2008**, *41*, 1653−1661.

(13) Giljohann, D. A.; Seferos, D. S.; Daniel, W. L.; Massich, M. D.; Patel, P. C.; Mirkin, C. A. Gold Nanoparticles for Biology and Medicine. *Angew. Chem., Int. Ed.* **2010**, *49*, 3280−3294.

(14) Lal, S.; Clare, S. E.; Halas, N. J. Nanoshell-Enabled Photothermal Cancer Therapy: Impending Clinical Impact. *Acc. Chem. Res.* **2008**, *41*, 1842−1851.

(15) Nikoobakht, B.; El-Sayed, M. A. Preparation and Growth Mechanism of Gold Nanorods (NRs) Using Seed-Mediated Growth Method. *Chem. Mater.* **2003**, *15*, 1957−1962.

(16) Jin, R. C.; Cao, Y. W.; Mirkin, C. A.; Kelly, K. L.; Schatz, G. C.; Zheng, J. G. Photoinduced Conversion of Silver Nanospheres to Nanoprisms. *Science* **2001**, *294*, 1901−1903.

(17) Pastoriza-Santos, I.; Liz-Marzan, L. M. Synthesis of Silver Nanoprisms in DMF. *Nano Lett.* **2002**, *2*, 903−905.

(18) Halas, N. J. Playing with Plasmons: Tuning the Optical Resonant Properties of Metallic Nanoshells. *MRS Bull.* **2005**, *30*, 362−367.

(19) Chen, J. Y.; Wiley, B.; Li, Z. Y.; Campbell, D.; Saeki, F.; Cang, H.; Au, L.; Lee, J.; Li, X. D.; Xia, Y. N. Gold Nanocages: Engineering Their Structure for Biomedical Applications. *Adv. Mater.* **2005**, *17*, 2255−2261.

(20) Erlebacher, J.; Aziz, M. J.; Karma, A.; Dimitrov, N.; Sieradzki, K. Evolution of Nanoporosity in Dealloying. *Nature* **2001**, *410*, 450−453.

(21) Bosman, M.; Anstis, G. R.; Keast, V. J.; Clarke, J. D.; Cortie, M. B. Light Splitting in Nanoporous Gold and Silver. *ACS Nano* **2012**, *6*, 319−326.

(22) Biener, J.; Nyce, G. W.; Hodge, A. M.; Biener, M. M.; Hamza, A. V.; Maier, S. A. Nanoporous Plasmonic Metamaterials. *Adv. Mater.* **2008**, *20*, 1211−1217.

(23) Yu, F.; Ahl, S.; Caminade, A. M.; Majoral, J. P.; Knoll, W.; Erlebacher, J. Simultaneous Excitation of Propagating and Localized Surface Plasmon Resonance in Nanoporous Gold Membranes. *Anal. Chem.* **2006**, *78*, 7346−7350.

(24) Ding, Y.; Chen, M. W. Nanoporous Metals for Catalytic and Optical Applications. *MRS Bull.* **2009**, *34*, 569−576.

(25) Fujita, T.; Guan, P. F.; McKenna, K.; Lang, X. Y.; Hirata, A.; Zhang, L.; Tokunaga, T.; Arai, S.; Yamamoto, Y.; Tanaka, N.; Ishikawa, Y.; Asao, N.; Erlebacher, J.; Chen, M. W. Atomic Origins of the High Catalytic Activity of Nanoporous Gold. *Nat. Mater.* **2012**, *11*, 775−780.

(26) Wittstock, A.; Zielasek, V.; Biener, J.; Friend, C. M.; Baumer, M. Nanoporous Gold Catalysts for Selective Gas-Phase Oxidative Coupling of Methanol at Low Temperature. *Science* **2010**, *327*, 319−322.

(27) Kelf, T. A.; Sugawara, Y.; Baumberg, J. J.; Abdelsalam, M.; Bartlett, P. N. Plasmonic Band Gaps and Trapped Plasmons on Nanostructured Metal Surfaces. *Phys. Rev. Lett.* **2005**, *95*, 116802.

(28) Lang, X. Y.; Qian, L. H.; Guan, P. F.; Zi, J.; Chen, M. W. Localized Surface Plasmon Resonance of Nanoporous Gold. *Appl. Phys. Lett.* **2011**, *98*, 093701.

(29) Sau, T. K.; Murphy, C. J. Room Temperature, High-Yield Synthesis of Multiple Shapes of Gold Nanoparticles in Aqueous Solution. *J. Am. Chem. Soc.* **2004**, *126*, 8648−8649.

(30) Huang, Y. J.; Wu, L.; Chen, X. D.; Bai, P.; Kim, D. H. Synthesis of Anisotropic Concave Gold Nanocuboids with Distinctive Plasmonic Properties. *Chem. Mater.* **2013**, *25*, 2470−2475.

(31) Ming, T.; Feng, W.; Tang, Q.; Wang, F.; Sun, L. D.; Wang, J. F.; Yan, C. H. Growth of Tetrahexahedral Gold Nanocrystals with High-Index Facets. *J. Am. Chem. Soc.* **2009**, *131*, 16350−16351.

(32) Ma, Y. Y.; Kuang, Q.; Jiang, Z. Y.; Xie, Z. X.; Huang, R. B.; Zheng, L. S. Synthesis of Trisoctahedral Gold Nanocrystals with Exposed High-Index Facets by a Facile Chemical Method. *Angew. Chem., Int. Ed.* **2008**, *47*, 8901−8904.

(33) Rodriguez-Fernandez, J.; Perez-Juste, J.; de Abajo, F. J. G.; Liz-Marzan, L. M. Seeded Growth of Submicron Au Colloids with Quadrupole Plasmon Resonance Modes. *Langmuir* **2006**, *22*, 7007−7010.

(34) Wang, H.; Halas, N. J. Mesoscopic Au "Meatball" Particles. *Adv. Mater.* **2008**, *20*, 820−825.

Supporting Information

Porous Au Nanoparticles with Tunable Plasmon Resonances and Intense Field Enhancements for Single-Particle SERS

Qingfeng Zhang[†], Nicolas Large[‡], Peter Nordlander[‡], and Hui Wang[†,*]

[†] *Department of Chemistry and Biochemistry, University of South Carolina, 631 Sumter Street, Columbia, South Carolina 29208*
[‡] *Department of Physics and Astronomy, Department of Electrical and Computer Engineering, and Laboratory for Nanophotonics, Rice University, Houston, Texas 77005*

* Corresponding author. Email: wang344@mailbox.sc.edu; Phone: 803-777-2203; Fax: 803-777-952.

S1. Experimental Details

Chemicals and Materials

Gold(III) chloride trihydrate (HAuCl$_4$·3H$_2$O, ACS grade) was obtained from J.T. Baker. Sodium borohydride (NaBH$_4$, 99%), L-ascorbic acid (AA, 99.5+%), hydrochloric acid (HCl, 37%) and poly(4-vinylpyridine) (PVP, Mw~60,000) were obtained from Sigma-Aldrich. (1-Hexadecyl)trimethylammonium chloride (CTAC, 96%) and 4-aminothiophenol (C$_6$H$_7$NS, 4-ATP, 97%) were obtained from Alfa Aesar. Hydrogen peroxide (H$_2$O$_2$, 30%), sulfuric acid (H$_2$SO$_4$, 96.10%), and ethanol (200 proof) were purchased from Fisher Scientific. All reagents were used as received without further purification. Ultrapure water (18.2 MΩ resistivity, Barnstead EasyPure II 7138) was used for all experiments. Silicon wafers were obtained from University Wafers.

Synthesis of Au Seeds

Colloidal Au seeds were prepared by the reducing HAuCl$_4$ with NaBH$_4$ in the presence of CTAC.[1] In a typical procedure, 0.30 mL of ice-cold, freshly prepared NaBH$_4$ (10 mM) were quickly injected into a solution composed of CTAC (10.00 mL, 0.10 M) and HAuCl$_4$ (0.25 mL, 10 mM) under magnetic stir. The seed solution was stirred for 1 min and then left undisturbed for 2 h. The seed solution was diluted 1000-fold with CTAC (0.10 M) and the diluted seed solution was used for the subsequent seed-mediated growth.

Synthesis of Au Porous Nanoparticles (PNPs)

The Au PNPs were prepared through a seed-mediated growth process. The growth solution was prepared by sequentially adding HAuCl$_4$ (0.50 mL, 10 mM) and AA (0.10 mL, 0.10 M) into a CTAC (10.00 mL, 0.10 M) solution. After gently mixing the growth solution for 30 s, the growth of Au PNPs was initiated by adding certain volumes of the diluted Au seed solution. The reaction solution was gently mixed for 30 s immediately after the addition of Au seeds and then left undisturbed at room temperature for 4 h. The as-obtained Au PNPs were washed with water three times through centrifugation/redispersion cycles, and finally redispersed in 5.0 mL of water. The overall sizes of the resulting Au PNPs were controlled by adjusting the amount of Au seeds added.

Synthesis of Au Quasi-Spherical (QS) Nanoparticles

The Au QS nanoparticles were fabricated following a similar protocol for the Au PNPs except for the addition of HCl. The growth solution was prepared by sequentially adding HAuCl$_4$ (0.50 mL, 10 mM), HCl (0.20 mL, 1.0 M) and AA (0.10 mL, 0.10 M) into a CTAC (10.00 mL, 0.10 M) solution. After gently mixing the reactants for 30 s, the growth of Au QS nanoparticles was initiated by adding certain volumes of the diluted Au seed solution. The reaction solution was gently mixed for 30 s immediately after the addition of Au seeds and then left undisturbed at room temperature for 4 h. The obtained Au QS nanoparticles were washed with water three times through centrifugation/redispersion cycles, and finally redispersed in 5.0 mL of water. The sizes of the Au QS nanoparticles could be controlled by adjusting the amount of Au seeds added.

Synthesis of Au Trisoctahedral (TOH) Nanoparticles

The Au TOH nanoparticles were fabricated following a similar protocol for the Au PNPs except for the increased amount of AA. The growth solution was prepared by sequentially adding HAuCl$_4$ (0.50 mL, 10 mM) and AA (1.0 mL, 0.10 M) into a CTAC (10.00 mL, 0.10 M) solution. After gently mixing the growth solution for 30 s, the growth of Au TOH nanoparticles was initiated by adding 0.01 mL of the diluted Au seed solution. The reaction solution was gently mixed for 30 s immediately after the addition of Au seeds and then left undisturbed at room temperature for 4 h. The obtained Au TOH

nanoparticles were washed with water three times through centrifugation/redispersion cycles, and finally redispersed in 5.0 mL of water.

Characterizations

The morphologies and structures of the nanoparticles were characterized by transmission electron microscopy (TEM) and selected area electron diffraction (SAED) using a Hitachi H-8000 transmission electron microscope operated at an accelerating voltage of 200 kV. All samples for TEM measurements were dispersed in water and drop-dried on 200 mesh Formvar/carbon-coated Cu grids. The structures of the nanoparticles were also characterized by SEM using a Zeiss Ultraplus thermal field emission scanning electron microscope. The samples for SEM measurements were dispersed in water and drop-dried on silicon wafers. The optical extinction spectra of the nanoparticles were measured on aqueous colloidal suspensions at room temperature, using a Beckman Coulter Du 640 spectrophotometer. Raman spectra and dark-field optical images were obtained on a Bayspec *Nomadic*[TM] Raman microscopy built on an Olympus BX51 microscope equipped with a 785 nm CW diode laser.

Single-Particle SERS Measurements

Sub-monolayer films of isolated Au particles were prepared by immobilizing the particles onto PVP(polyvinylpyridine)-functionalized silicon substrates.[2] In a typical procedure, silicon substrates were cleaned in a piranha solution (sulfuric acid : hydrogen peroxide, 7 : 3) for 15 min, and then immersed in a 1% wt. of PVP ethanolic solution for 24 h. The silicon substrates were thoroughly rinsed with ethanol, dried with N_2 gas, and then immersed in an aqueous solution of Au particles for 1 h. The silicon substrates were thoroughly rinsed with ethanol and dried with N_2 gas after they were removed from the solution of Au particles. The coverage of Au particles on the substrates can be controlled by changing the immersion time.

The samples for single-particle SERS experiments were prepared by evaporating 20 μL of a 1.0 mM ethanolic solution of 4-ATP on the surface of the isolated Au particles on PVP-functionalized silicon substrates. The substrates were then thoroughly rinsed with ethanol and dried with N_2 gas. A couple of drops of water were dropped onto the substrates to ensure that the surrounding medium of the Au particles was water, and then a clean glass slide with a 0.17 mm thickness was covered onto the top of the water layer before the Raman spectral collection. The distance between silicon substrate and the glass slide is about 0.5 mm. Figure S4A shows the scheme of the substrate geometry of the single-particle SERS measurements. SERS spectra were obtained on a Bayspec *Nomadic*[TM] Raman microscopy built on an Olympus BX51 reflected optical system under 785 nm laser excitation in the confocal mode (focal area of 2 μm diameter). A 50× dark field objective (NA=0.5, WD=10.6 mm, Olympus LMPLFLN-BD) was used for both Raman signal collection and dark field scattering imaging. The laser beam was focused on one particle each time for Raman spectrum collection. The laser power focused on the samples was measured to be 3.6 mW and the spectrum acquisition time was 20 s. Normal Raman spectra of 4-ATP were collected on solid films of neat 4-ATP on the silicon wafers under the same conditions.

Enhancement Factor (EF) Calculations

We estimated the enhancement factors (EFs) of Raman signals using the following equation:

$$EF = (I_{SERS} \times N_{normal}) / (I_{normal} \times N_{SERS}),$$

where I_{SERS} is the intensity of a specific band in the SERS spectra of 4-ATP; I_{normal} is the intensity of the same band in the normal Raman spectra of 4-ATP under the same condition; N_{normal} is the number of probe molecules in the excitation volume for the normal Raman measurements; N_{SERS} is the number of adsorbed molecules on an individual particle. Two Raman modes of 4-ATP at 1078 cm^{-1} and 1590

cm^{-1} were chosen for the EF calculations. To estimate the N_{normal}, we calculated the effective excitation volume by using the following equation: $V = \pi \times (d/2)^2 \times H$, where d is the diameter of the beam size (d = 2 μm) and H is the effective depth of focus (H= 10 μm, which was estimated by finely controlling the height of the stage during the Raman measurement of silicon wafers). Thus, we estimated an effective excitation volume of 3.14×10^{-17} m^3 for our Raman microscopy with 785 nm excitation using the 50× objective. Then N_{normal} was calculated by using the following expression: $N_{normal} = (V \times D/M) \times N_A = 1.80 \times 10^{11}$ molecules, where D is the density of 4-ATP (1.17 g/mL), M is the molar mass of 4-ATP (125 g/mol) and N_A is the Avogadro constant (6.02×10^{23} mol^{-1}). To determine N_{SERS}, a self-assembled monolayer of 4-ATP molecules (molecular footprint size of 0.39 nm^2) [3] was assumed to be closely packed on the surface of each Au particle. The surface area of the particle was estimated by assuming that each Au PNP has four times of the surface area than a smooth sphere of the same overall size. For instant, a Au PNP with the diameter of 2R=189 nm: S=16×π×R^2 nm^2 = 448656 nm^2, and then N_{SERS} = S/0.39 = 1.15×10^6 molecules. In this way we were able to estimate the N_{SERS} values for particles with different size and then calculate the EFs.

Finite-Difference Time-Domain (FDTD) Calculations

FDTD simulations (FDTD, Lumerical Solutions) were performed to calculate the far-field and near-field properties of the Au nanoparticles. Dielectric permittivity tabulated by Johnson and Christy[4] was used for Au and a refractive index of 1.34 was used for water.[5] The geometric parameters used in the simulations for the Au PNPs, smooth spherical, and TOH nanoparticles were extracted from the experimental TEM and SEM images. The Au PNPs and the smooth spherical particles were 67, 108, 135, 165, 189, and 215 nm in diameter, while the side length of the TOH particle was 94 nm. N spherical pores ranging from 10 to 40 nm in diameter were generated and distributed randomly at the surface of the spherical nanoparticles. The number of pores, N, increased with the nanoparticle size, in agreement with experimental observations. The random distribution of the pores allowed the formation of larger craters at the nanoparticle surface and craters with random depths, thus showing a good morphological agreement with the actual particle geometry. To account for the small morphological details and ensure a good numerical convergence, a uniform FDTD meshgrid of 2 nm was used.

Extinction spectra were calculated by averaging three incident polarizations. This allowed us to reproduce the orientation averaging, the random pore distribution, and unpolarized-light excitation of the experimental configuration. Near-field enhancement distributions ($|E/E_0|^2$) were calculated at 785 nm for a given incident polarization. The near-field ($|E/E_0|^2$ and $|E/E_0|^4$) were spatially integrated over a spherical volume of radius R+1 nm where R was the radius of the nanoparticle. The mean enhancements, $<|E/E_0|^2>$ and $<|E/E_0|^4>$ with the unit of nm^{-3}, were calculated by normalizing the integrated $<|E/E_0|^2>$ and $<|E/E_0|^4>$ over the integration volumes.

References
(1) Zhang, J.; Langille, M. R.; Personick, M. L.; Zhang, K.; Li, S. Y.; Mirkin, C. A. *J. Am. Chem. Soc.* **2010**, *132*, 14012.
(2) Wang, H.; Halas, N. J. *Adv. Mater.* **2008**, *20*, 820.
(3) Mohri, N.; Matsushita, S.; Inoue, M.; Yoshikawa, K. *Langmuir* **1998**, *14*, 2343.
(4) Johnson, P. B.; Christy, R. W. *Phys. Rev. B* **1972**, *6*, 4370.
(5) Hale, G. M.; Querry, M. R. *Appl. Optics.* **1973**, *12*, 555.
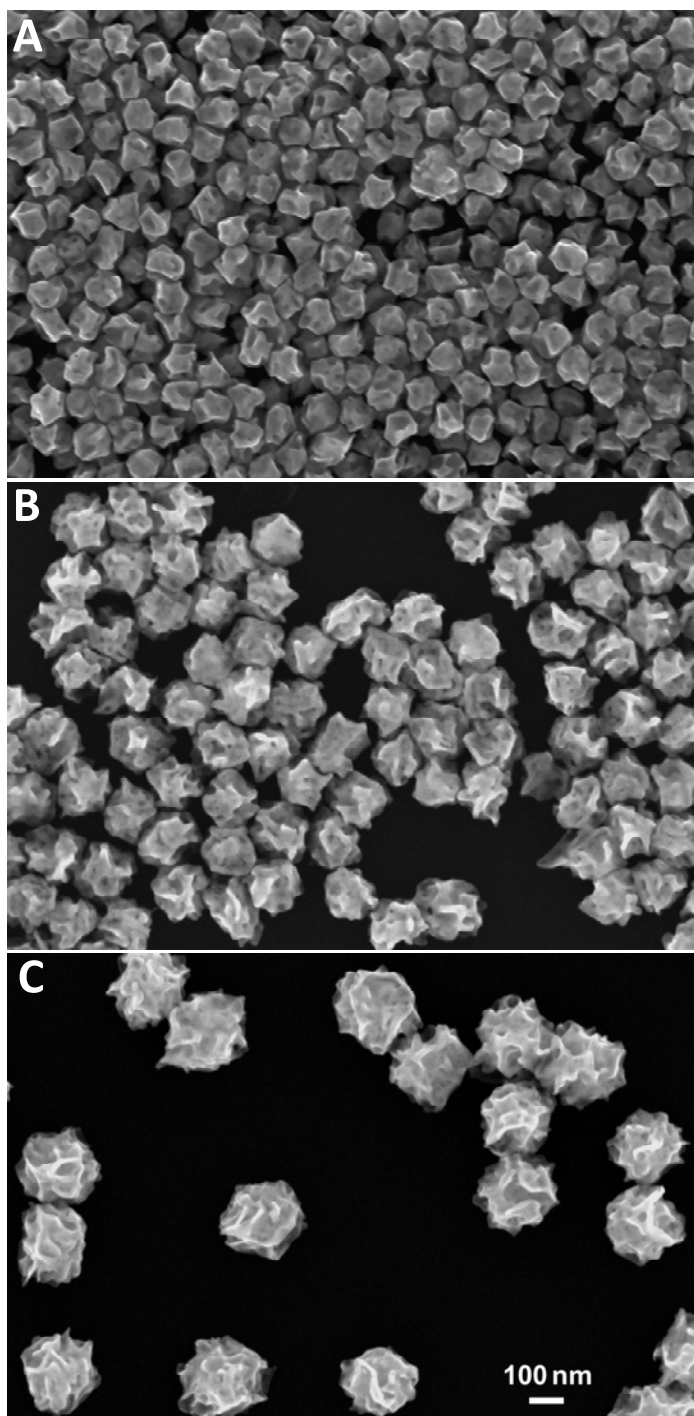
S2. Additional Figures

Figure S1. SEM images of the Au PNPs with overall diameters of (A) 108 $\pm$ 6 nm; (B) 165 $\pm$ 7 nm; (C) 215 $\pm$ 12 nm. All the images share the same scale bar in Panel C.
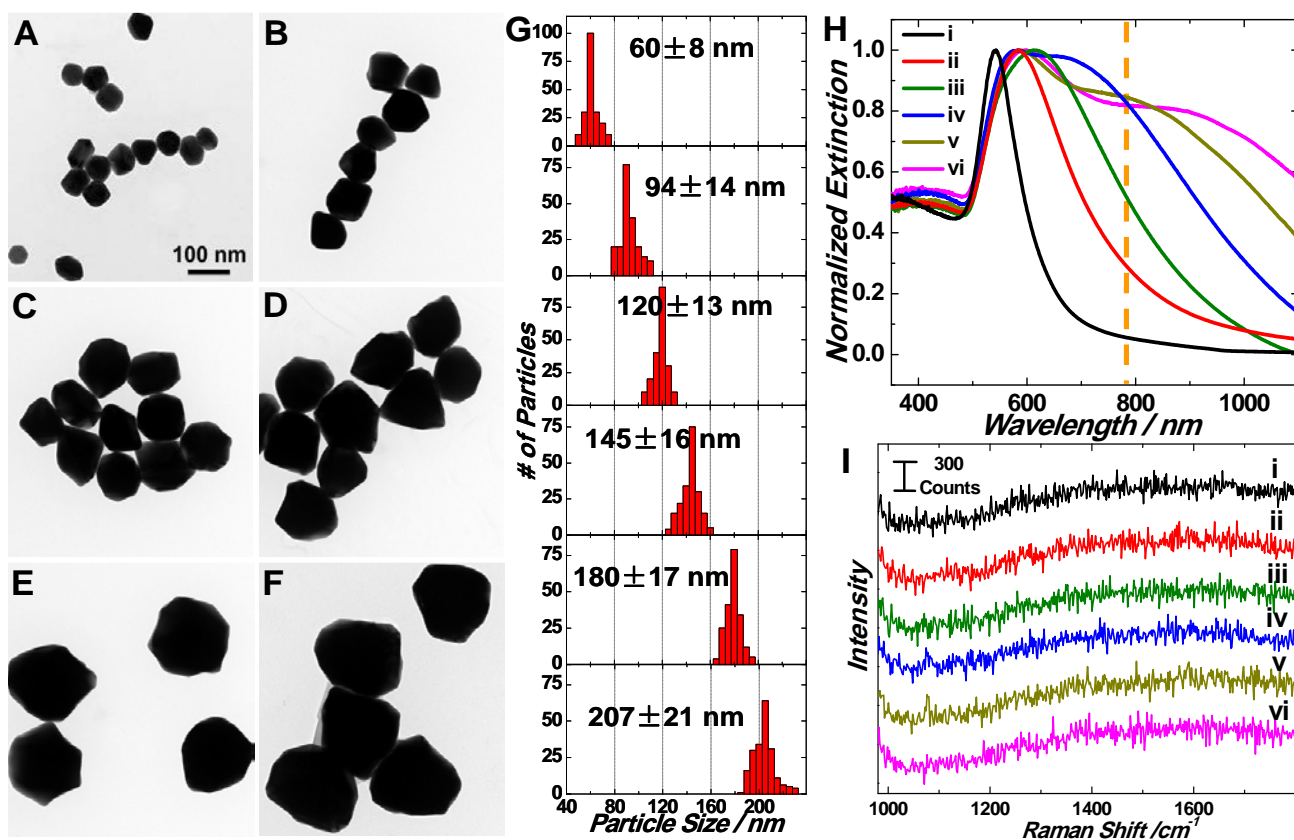
Figure S2. TEM images of quasi-spherical Au nanoparticles with controllable average sizes fabricated by adding (A) 0.5 mL, (B) 0.1 mL, (C) 0.05 mL, (D) 0.025 mL, (E) 0.015 mL, and (F) 0.01 mL of Au seed solution. All TEM images share the same scale-bar in panel A. (G) Histograms showing the size distributions of the quasi-spherical Au nanoparticles shown in panels A-F. (H) Experimental extinction spectra of the quasi-spherical Au particles with different sizes shown in panels A-F. The vertical dashed line shows the excitation laser wavelength (785 nm) for Raman measurements. (I) Representative SERS spectra of 4-ATP adsorbed on individual quasi-spherical Au nanoparticles. The labels of i to vi correspond to the samples shown in panels A-F, respectively.
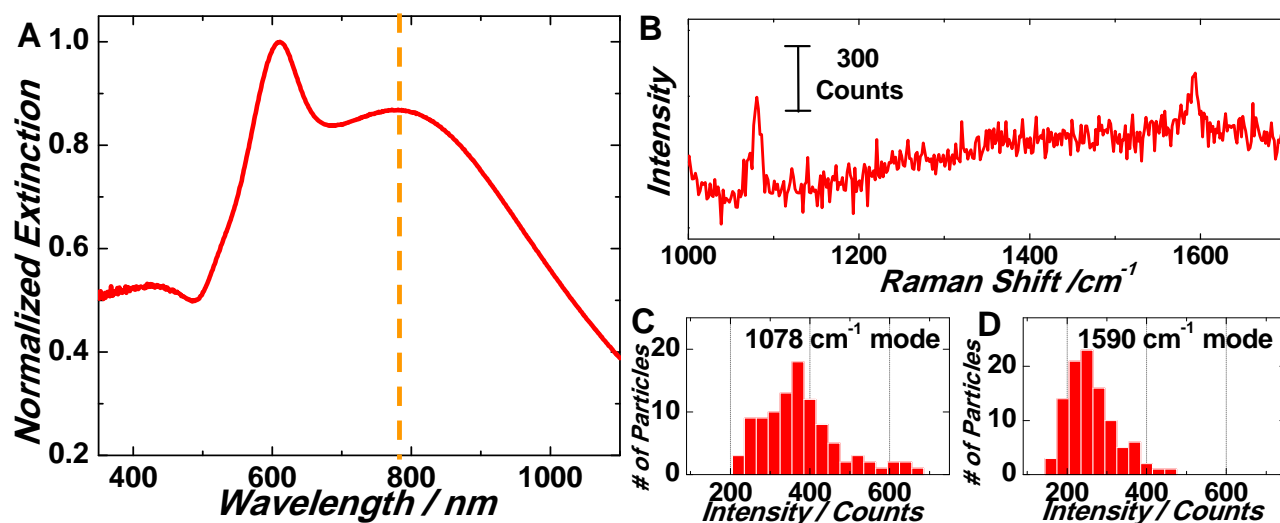
Figure S3. (A) Experimental extinction spectrum of colloidal trisoctahedral (TOH) Au nanoparticles. The vertical dashed line shows the excitation laser wavelength (785 nm) for Raman measurements. (B) Representative SERS spectrum of 4-ATP adsorbed an individual TOH Au nanoparticle. Histograms of the Raman intensities of (C) 1078 cm^{-1} mode and (D) 1590 cm^{-1} mode of 4-ATP adsorbed on individual TOH Au nanoparticles.
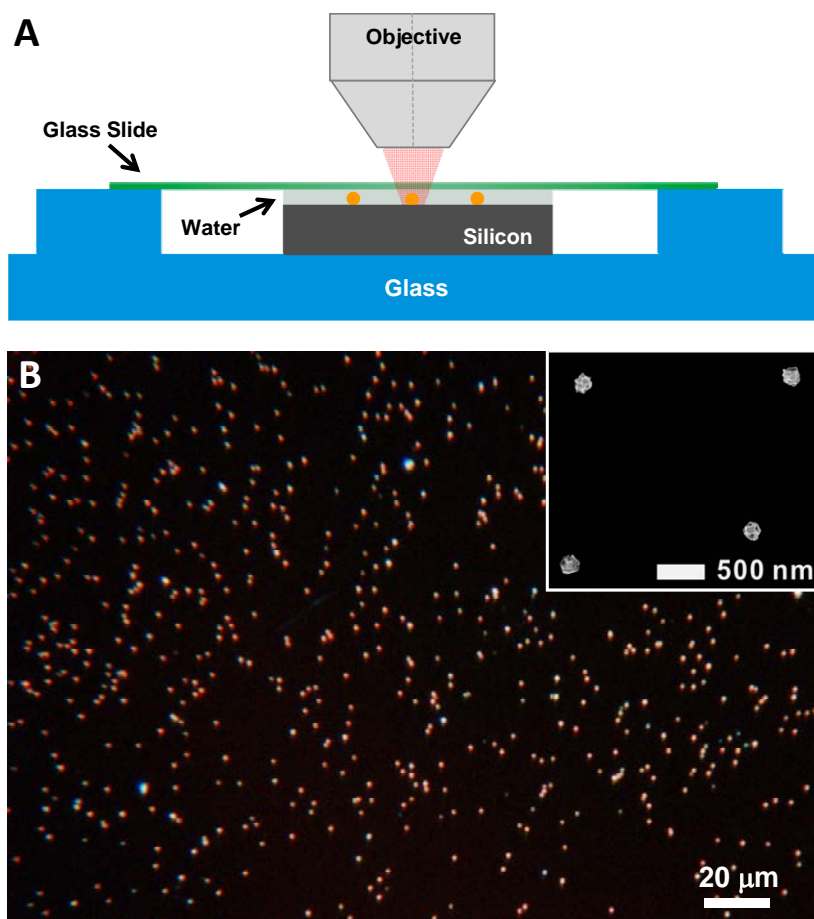
Figure S4. (A) Schematic illustration of the single-particle SERS measurements on individual Au PNPs using the confocal Raman microscope. (B) Dark-field optical image and (inset) SEM image of a sub-monolayer of isolated Au PNPs immobilized on poly(vinylpyridine)-functionalized silicon substrate for single-particle SERS measurements.
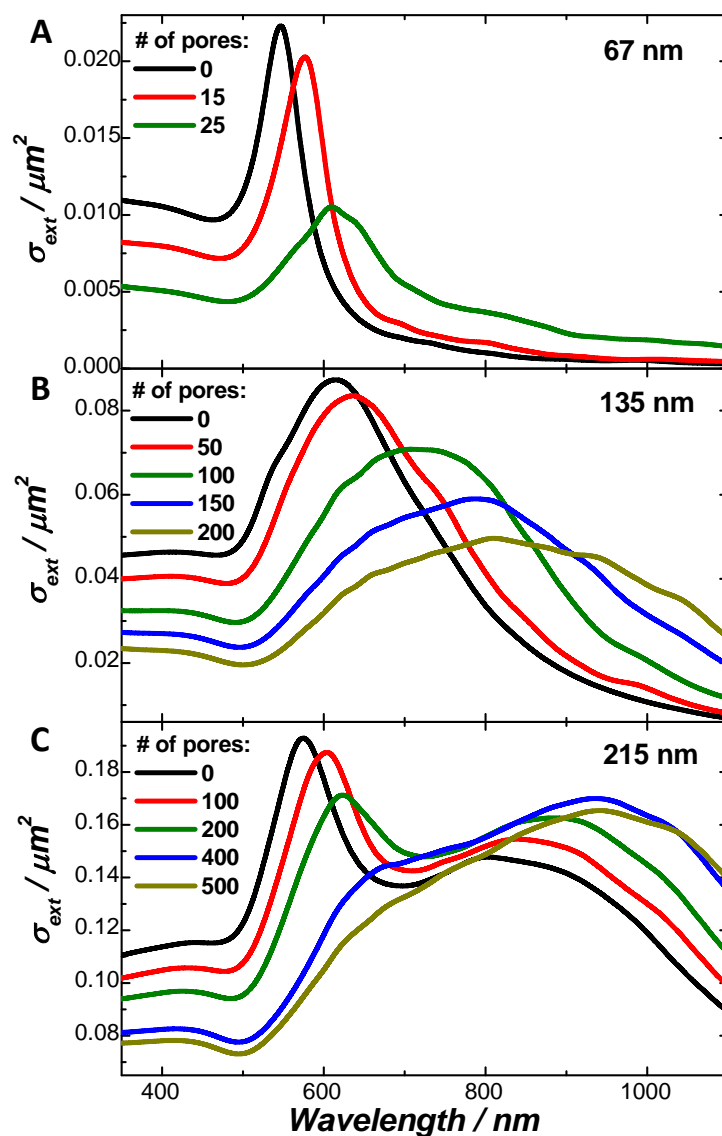
Figure S5. Calculated extinction spectra showing the effects of number of pores on the optical properties of the spherical Au particles. The overall diameters of the particles are (A) 67 nm, (B) 135 nm, and (C) 215 nm, respectively. The numbers of pores added to each particle are labeled in each panel.
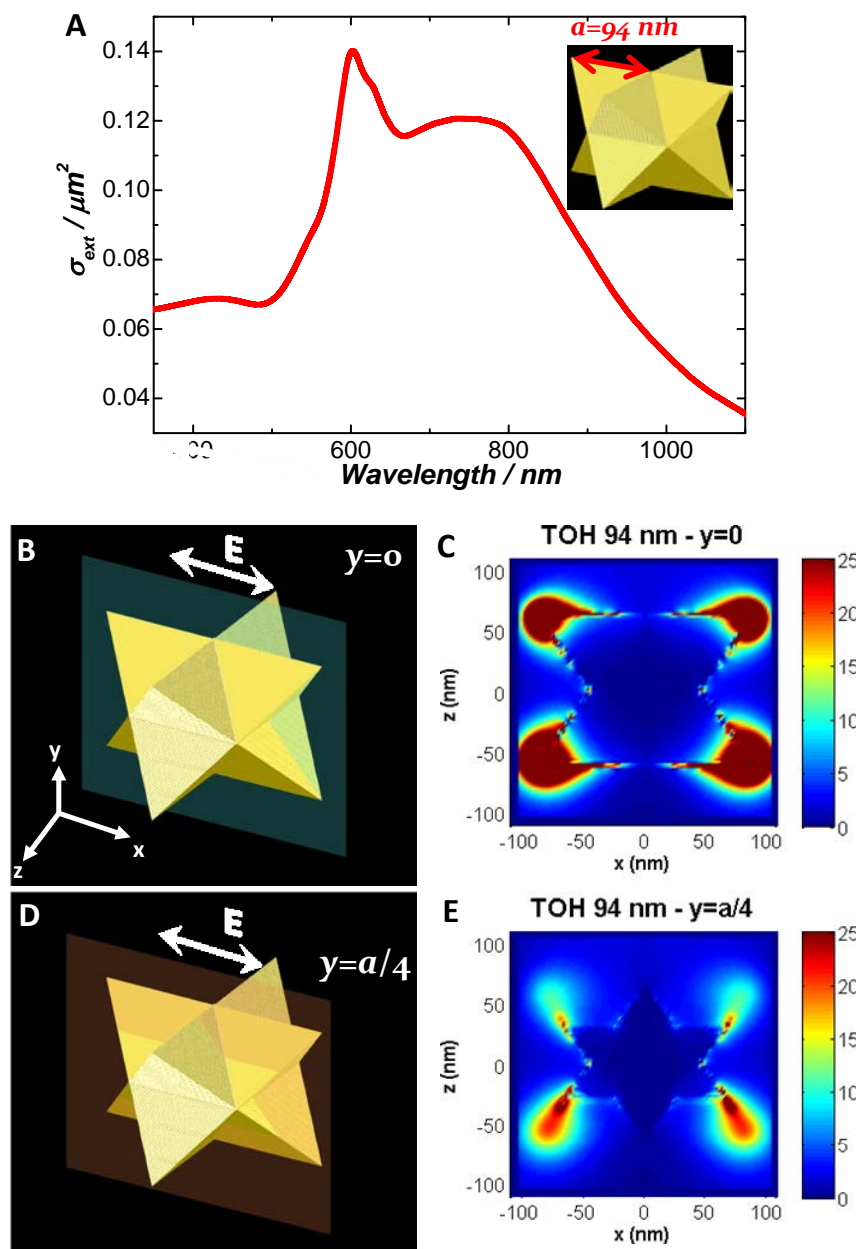
Figure S6. (A) Calculated extinction spectrum of a Au TOH nanoparticle with side length (*a*) of 94 nm. The inset is the 3D illustration of the geometry of Au TOH. Schematics showing the cross-sections of the TOH particle and the calculated near-field ($|E/E_0|^2$) plots (B,C) at y=0 plane and (C, D) at y= a/4 plane.